Thermal Science and Engineering Progress 55 (2024) 102978

Contents lists available at ScienceDirect

Thermal Science and Engineering Progress

journal homepage: www.sciencedirect.com/journal/thermal-science-and-engineering-progress

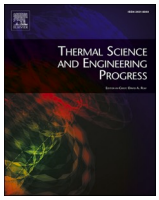

Experimental evaluation of green nanofluids in heat exchanger made oF PDMS

Glauco Nobrega [a,b,*], Reinaldo Souza [a,c], Beatriz Cardoso [a], Inês Afonso [a], José Pereira [c], Elaine Cardoso [d,e], Ana Moita [c,f], João Ribeiro [b], Rui Lima [a,g,h]

[a] Mechanical Engineering and Resource Sustainability Center (MEtRICs), Mechanical Engineering Department, University of Minho, Campus de Azurém, 4800-058 Guimarães, Portugal
[b] Centro de Investigação de Montanha (CIMO), Campus de Santa Apolónia, Instituto Politécnico de Bragança, 5300-253 Braganca, Portugal
[c] IN+, Center for Innovation, Technology and Policy Research, Instituto Superior Tecnico, Universidade de Lisboa, Av. Rovisco Pais, 1049-001 Lisboa, Portugal
[d] UNESP - São Paulo State University, School of Engineering, Ilha Solteira, SP, 15385-000, Brazil
[e] UNESP - São Paulo State University, School of Engineering, São João da Boa Vista, Brazil
[f] CINAMIL—Centro de Investigação Desenvolvimento e Inovação da Academia Militar, Academia Militar, Instituto Universitário Militar, Rua Gomes Freire, 1169-203 Lisboa, Portugal
[g] Transport Phenomena Research Center (CEFT), Faculdade de Engenharia da Universidade do Porto (FEUP), Rua Roberto Frias, 4200-465 Porto, Portugal
[h] Associate Laboratory in Chemical Engineering (ALiCE), Faculty of Engineering, University of Porto, 4200-465 Porto, Portugal

ARTICLE INFO

Keywords:
Green nanofluids
PDMS exchanger
Thermal conductivity
Stability

ABSTRACT

Conventional methods for synthesizing metallic nanoparticles face challenges such as instability and environmental concerns. Therefore, new, simpler, and more eco-friendly methods are being explored. In this context, the study reports a green synthesis process to produce magnetic iron oxide nanoparticles using an aqueous extract of the alga *Chlorella vulgaris*. This process leverages natural resources to create a sustainable nanofluid known as green nanofluid. To evaluate the characteristics of this nanofluid, experimental measurements of wettability, viscosity, thermal conductivity, and qualitative stability analysis were conducted. An experimental setup consisting of a heat exchanger made of polydimethylsiloxane (PDMS) was used to assess the thermal performance and the results were compared to theoretical equations and numerical simulation. Additionally, thermographic imaging of temperature gradients as the fluids passed over the heated surface of the serpentine channel were made. The main findings confirmed that the nanofluid was more stable than that obtained by traditional methods and had a more uniform temperature distribution over the heat exchanger. The higher concentration exhibited superior thermal performance compared to DI-Water. Moreover, the green nanofluid was used at a weight concentration of 0.1 wt%, provided thermal performance results of nearly 4.5% superior to those estimated by the numerical model and 6.4% higher than those experimentally obtained with the base fluid, respectively. Finally, the results obtained for the nanofluid also showed an average increase of around 5% in the viscosity of the base fluid, with a more significant sedimentation at a concentration of 0.1 wt%.

1. Introduction

Recent advances in nanomaterial research have enabled the exploration of new materials that may be more effective in enhancing heat transfer. The production of nanoparticles (NPs) has been prominent since it is used in different application areas such as medicine, electronics, sensor applications, chemical induction, and electrochemical applications, representing a promising technology for applications of high complexity and performance, such as those found in the aerospace industry [1]. Nanoparticles encompass a diverse range of materials and consist of particles with a dimension smaller than 100 nm [2].

Those produced from metal precursors, such as iron, zinc, copper, gold, cobalt, nickel, and other stable metals [3], are known as metallic NPs. Their versatility is advantageous as their thermal, optical, magnetic, plasmonic, and catalytic properties can be adjusted according to their size, composition, and shape [4,5]. In addition to these characteristics, metallic NPs are associated with biological attributes, such as antibacterial, antifungal, and anticancer properties [6]. This class of nanoparticles can be synthesized by physical, chemical, and biological

* Corresponding author.
E-mail address: nobregaglauco@gmail.com (G. Nobrega).

https://doi.org/10.1016/j.tsep.2024.102978
Received 12 September 2024; Received in revised form 8 October 2024; Accepted 10 October 2024
Available online 18 October 2024

Nomenclature

c_p	Specific heat capacity, (J/kgK)
D_h	Hydraulic diameter, (mm)
f	Fully developed friction factor, (−)
f_{app}	Apparent friction factor, (−)
G	Function of the channel aspect ratio, (−)
H_{ch}	Channel height, (mm)
k	Thermal conductivity, (W/m • K)
L	Length of the test section channel, (m)
L^+	Hydraulic channel length, (−)
r	Ratio
$\dot{m}$	Mass flow rate, (kg/s)
n	Shape factor, (−)
p	Order of convergence
Δp	Pressure drop, (Pa)
Q	Volumetric flow rate, (ml/min)
$\dot{Q}$	Heat flux, (W)
Re	Reynolds number, (−)
T	Temperature, (°C)
v	Velocity, (m/s)
w	Sphericity of the particle, (−)
W_{ch}	Channel width, (mm)
W_p	Distance between channels, (mm)

Greek letters

φ	Particle volume Concentration, (w/v%)
μ	Viscosity, (mPas)
θ	Contact angle, (°)
ρ	Density, (kg/m3)
$\mathcal{Q}$	Evaluated parameter
ξ	Relative error

Subscripts

bf	Base fluid
np	nanoparticles
H&C	Hamilton & Crosser
Maxwell	Maxwell

methods [7]. Although physical and chemical methods are more widely explored and described in the literature [8], some actual limitations and challenges, including lack of stability, use of toxic precursors and organic solvents, large waste production, need for high pressures and temperatures, and excessive energy consumption [9,10].

These limitations allow for exploring environmentally friendly and advantageous synthesis methods, as with green syntheses that have been the focus of scientific study in recent years. These methods utilize a variety of natural resources, such as plants, algae, fungi, bacteria, and yeasts, available on the planet, which act as reducing agents and stabilizers in the synthesis of metallic nanoparticles, allowing them to overcome many of the limitations of conventional methods.

When added to a base fluid, these NPs form nanofluids. Although the applications of nanofluids range from drug delivery and lubrication to antimicrobial activity [2,3], it is in heat exchange systems that they stand out, offering more efficient and sustainable solutions for thermal engineering [11]. They can be used in any equipment using thermal fluids, including heat pipes, solar collectors, radiators, and pumped cooling systems, involving phase change or not [4,12]. Some relevant literature includes studies conducted by researchers Ajeeb and Murshed [13], who performed experimental and numerical analyses on the heat transfer performance of nanofluids. In other works, they analyzed the heat transfer performance of nanofluids containing aluminum and alumina [14], silica, titania, and boron nitride [15,16] in heat exchangers with mini- and microchannels.

Moreover, technologies with rapidly increasing processing capacity can benefit from advances in the sector. That is the case with high-power electronic devices such as Central Processing Units (CPUs) and Graphics Processing Units (GPUs), which generate intense heat, leading to overheating problems and even system failures. Thus, the heat dissipation procedures play a pivotal role in maintaining the reliability of this equipment [17].

However, nanoparticles in the base fluid can modify its surface tension and, consequently, its wettability and alter viscosity and thermal conductivity, which are crucial parameters for adequate application in heat transfer systems. For example, wettability mainly influences the heat exchangers operating under flow boiling conditions, affecting effective heat exchanges and fluid transport driven by capillarity. Also, viscosity plays a significant role, especially in mechanical pumping systems, due to the fluid's resistance to flow and subsequent pressure loss. Thermal conductivity is essential for enhancing the heat transfer of nanofluids when the surface is cooled. Moreover, it is essential to achieve a stable nanofluid solution that can prevent nanoparticle aggregation and sedimentation [3,18].

Within this context, this work aims to report the thermal performance of nanofluids containing magnetite nanoparticles synthesized through a process known as green synthesis. The analysis includes the evaluation of the wettability, viscosity, thermal conductivity, and stability obtained through measurement techniques widely consolidated in the literature. A serpentine-type heat exchanger made of PDMS (polydimethylsiloxane) was also used to assess the nanofluid's capacity in a thermal system. PDMS is an elastomer widely used in microfluidic or lab-on-a-chip applications. The fabrication process, its lightweight, and its ability to enable the manufacture of heat sinks with complex topologies and geometries justified its choice [19].

Chlorella vulgaris algae extract was used for the green synthesis of nanoparticles. The use of algae in synthesizing metallic nanoparticles is possible with different species of algae [20–22], this being one of them. The choice of preparation method, instead of a traditional technique, lies in the fact that combining these nanoparticles with algae extract is believed to be a simple and economical way to increase the long-term stability of nanofluids, as found by [20,22].

Copeland's theoretical model [23] was used for the pressure drop, and the results were compared with those of the numerical simulation using commercial ANSYS CFD software (ANSYS, Inc.).

The novelty of the current study is closely linked with the innovative synthesis of the nanoparticles of the employed eco-friendly nanofluid. Based on the authors' knowledge, this is the first time algae extract-based nanoparticles have been used in the operating nanofluid of a heat exchanger for heat transfer enhancement purposes. Also, the present experimental and numerical analysis aims to provide valuable insights for optimizing thermal management systems based on PDMS frames and environmentally friendly operating nanofluids.

2. Materials and methods

2.1. Preparation of the samples

2.1.1. Method for obtaining the PDMS serpentine

Another of our works details the method for obtaining the PDMS serpentine [24]. In summary, resin was chosen for mold fabrication due to its superior printing quality and finer, smoother finish. Next, the PDMS Sylgard® 184, a polymeric component, and a curing agent, were used at a ratio of 10:1, respectively, with materials mechanically mixed for about 10 min. Subsequently, the mixture was degassed using a vacuum pump for about 30 min, and finally, the solution was poured

into the mold. The PDMS curing process occurs in an oven for 2 h at 60 °C. Lastly, the serpentine was carefully removed from the mold using a spatula.

2.1.2. Preparation of Chlorella vulgaris extract

Chlorella vulgaris was obtained from ALLMA®. The pH value was measured using an APERA Instruments PH20 pH meter, and the pH of each solution was appropriately adjusted using a 1 M solution of sodium hydroxide (NaOH) sourced from Sigma-Aldrich, St. Louis, MO, USA.

7.5 g of Chlorella *vulgaris* algae powder was added to 100 mL of distilled water to prepare the aqueous extract. The solution was heated to 55 °C and stirred magnetically for 24 h. Subsequently, the solution was centrifuged at 6000 rpm for 20 min to separate biological residues from the extract. The resulting supernatant from centrifugation was then filtered through Whatman N°.1 filter paper. The aqueous extract was stored at 4 °C for future use.

2.1.3. Preparation of iron oxide nanoparticles using Chlorella vulgaris extract

In order to synthesize the nanoparticle, a volume of 4 mL of the previously prepared *Chlorella vulgaris* aqueous extract was added to a 100 mL solution of 0.2 M of iron (II) chloride. The algal extract and iron chloride solution were allowed to react for 20 min and incubated at 60 °C to initiate the first reduction reactions of iron chloride using natural reducing agents from the algal extract. Subsequently, the pH of the reaction mixture was adjusted to pH = 11 using 1 M of NaOH. Various aliquots corresponding to reaction times of 0.5 h, 2 h, and 6 h were collected.

The ultraviolet absorption spectrum of the aliquots was analyzed, and the formation of an absorbance peak indicated the formation of nanoparticles. Within 30 min, the solution turned dark brown, indicating the production of iron oxide nanoparticles. The synthesized nanoparticles were then isolated via centrifugation (6000 rpm at room temperature for 20 min). The supernatant was discarded, and the nanoparticle pellet was resuspended in distilled water. This process was repeated twice to eliminate any by-products of the reaction and cleanse the surface of the nanoparticles. The bio-reduction of iron ions to magnetic iron nanoparticles was monitored by measuring UV–VIS spectra of the aliquots at intervals of 0.5 h, 2 h, and 6 h using a UV-1800 UV–Vis Spectrophotometer.

In order to measure the weight concentration of nanoparticles, the nanofluid was sonicated for 20 min to enhance dispersion within the fluid. Subsequently, 5 g of the nanofluid was added to a glass beaker with a known mass. The filled beaker was then dried at 60 °C in an oven, and the weight was measured again using a high-precision scale. With this value, the concentration of nanoparticles was determined. Distilled water was then added to obtain the desired concentrations.

2.2. Characterization of the samples

2.2.1. Biosynthesis of Fe_3O_4 NPs and UV–vis spectroscopy

The synthesis of Fe_3O_4 NPs was visually monitored by observing a color change in the reaction mixture, consisting of iron chloride salts and *Chlorella vulgaris* aqueous extract, upon adding NaOH (pH = 11). The color change, shifting from light brown to dark brown over time, provides empirical evidence of the successful synthesizing of Fe_3O_4 NPs. Subsequently, the separation of Fe_3O_4 NPs was achieved through magnetic separation, facilitated by applying an external permanent magnet at the end of the reaction. To determine the optimal reaction time for synthesis, several aliquots were extracted at intervals of 0.5 h, 2 h, and 6 h.

2.2.2. Wettability

The wettability of each fluid was assessed using the DataPhysics OCA − Series instrument with an accuracy of ± 0.1° at room temperature (20 °C). Samples were evaluated on three different substrates: glass (Microscope slides VWR®), PDMS manufactured according to [7,24], and aluminum (AL6070-T6, roughness 4.489 μm). Drops of each fluid, with a volume of 10 μL, were dispensed, and twenty-four samples were taken for each fluid at six different positions.

2.2.3. Viscosity measurements

The viscosity of the fluids was determined using a rotational rheometer MCR 92 Anton Paar with an accuracy of 1 %. A cone-plate geometry with a diameter of 50 mm and a 1 mm gap was employed. Steady shear flow curves were obtained at a constant temperature of 20 °C. Three replicates of each measurement were performed to ensure reproducibility.

2.2.4. Stability tests

The stability tests of the green nanofluid, produced from algae extract, were carried out by obtaining optical images for a concentration of 0.1 wt% within a time window of 5 h. To compare the stability of the nanoparticles after the suggested time interval, another nanofluid of the same concentration, but made without the algae extract, was prepared.

2.2.5. Thermal conductivity measurements

Thermal conductivity measurements were carried out using the transient plane source method with a Hot Disk TPS 2500S instrument with an accuracy of 5 %. The Hot Disk 5501 F1 sensor was used, and the fluid was enclosed within a PDMS cell designed for NF thermal conductivity measurements, as described in [7]. Measurements were conducted with concentrations from 0.05 and 0.1 wt% of magnetic nanoparticles and were compared with the DI-Water base fluid.

2.3. Experimental setup of heat transfer experiment

Fig. 1 schematically represents the experimental setup and the interconnection between equipment and components. A *Harvard Apparatus® 22* syringe pump (1) was used to pump the working fluid into the system containing the test section (2), where it was heated by a stainless-steel sheet and subsequently stored in the reservoir (3).

The heat flux was induced by adjusting the electric current from the power supply using Axio Met® AX-3020L 20VDC 20A DC (4), which was fine-tuned to the desired values based on readings from a multimeter, PCWork® (5). Inlet (T_{in}) and outlet (T_{out}) fluid temperatures were tracked using two type-T thermocouples linked to a DT9829 data acquisition board (6). In contrast, the pressure variance between the inlet and outlet was gauged by an Omega® PX409-005DWUV pressure sensor (7). This sensor was connected to the data acquisition board and powered by a Leybold® 521 45 power supply (8). The temperature distribution across the stainless-steel sheet was observed through an Onca MWIR-InSb-320 thermographic camera (9) positioned beneath the serpentine channel, facing upwards with the focus adjusted manually. This equipment choice allows temperature gradients of the heated surface to be obtained without any interference, either from the liquid flow crossing the serpentine channel or needing a local sensor.

Additionally, at the center of the surface, immediately below the serpentine flow channel on the external part of the stainless-steel sheet, a T-type thermocouple was positioned to monitor the temperature of the wall (T_S) in that region. The temperature measured by this thermocouple was used in the thermal heat transport equations described in this study. Furthermore, the values of the thermocouple served as a reference for calibrating the thermal camera. Finally, a computer (10) recorded the temperature and pressure signals for the subsequent analysis of results. Fig. 2 shows details of the arrangement where the testing section was located.

The arrangement containing the test section consists of a flat wooden board (1) with a circular hole 10 mm in diameter to facilitate the monitoring of the surface temperature through the thermographic camera. The viewing window allowed the direct filming of the heating surface in contact with the flowing liquid. On top of the wooden board, a

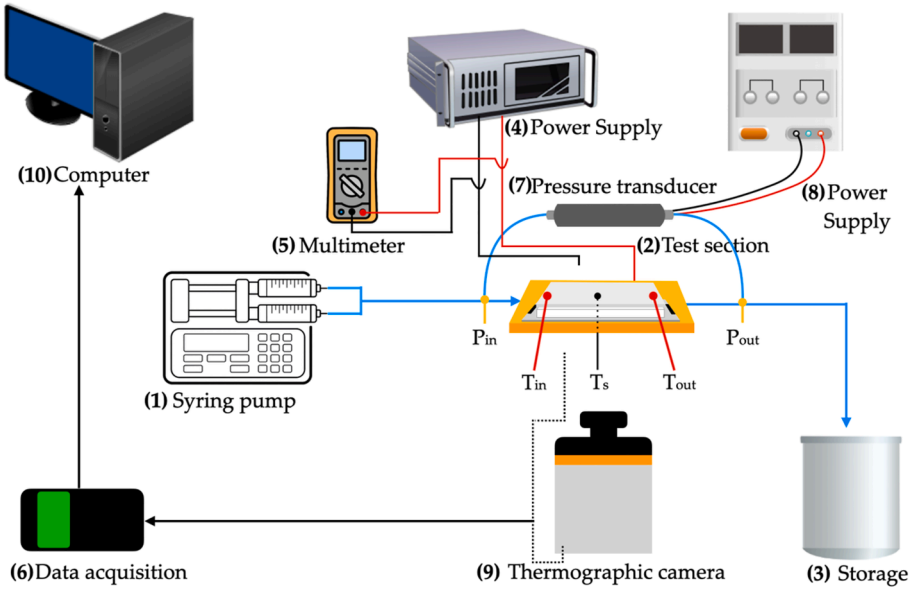

Fig. 1. Schematic diagram of the experimental setup.

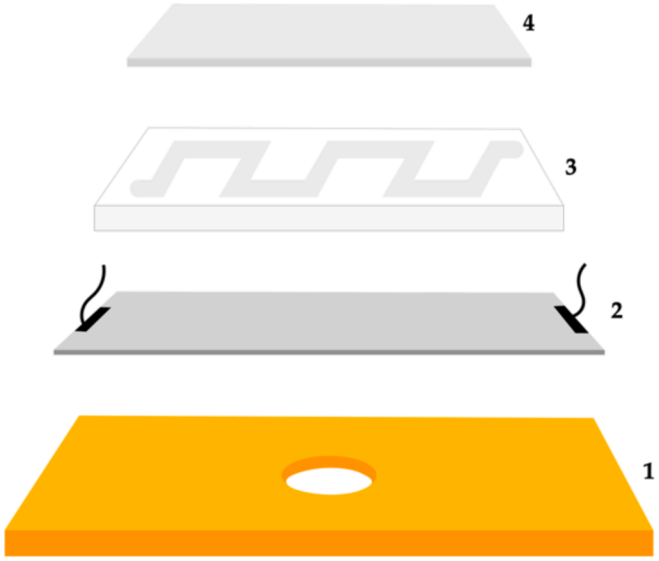

Fig. 2. Scheme of the arrangement containing the test section. (1) wooden board with a circular hole, (2) heating surface and electrical connections, (3) PDMS serpentine, (4) acrylic piece to fix all the elements to the wooden board.

thin sheet of commercially available AISI304 stainless steel (2) with a thickness of 20 μm and dimensions of 65 mm × 65 mm was positioned just below the PDMS serpentine (3). Two wires for the electrical supply were fixed at the ends of the heating plate. These wires were connected to the power source that heated the plate, imposing a constant heat flow through the Joule effect. The PDMS serpentine (3) was placed on the heating plate with the liquid flow channel facing it. Finally, a piece of acrylic (4) secured the entire assembly to the wooden board.

It should be noted that the flexibility and malleability of the PDMS allowed the system to be completely sealed. Therefore, in this experimental setup, the fluid is pumped into the serpentine heat exchanger using a syringe pump. At the serpentine's inlet, the temperature and pressure of the fluid are measured. As the fluid flows through the serpentine, it is heated by a stainless-steel sheet, which is connected to a power supply and generates heat through the Joule effect, with a power input of 6 W. Upon exiting the serpentine, the temperature and pressure of the fluid are measured again. Finally, the fluid is directed into a reservoir for storage without undergoing recirculation.

The side of the steel sheet facing the thermal camera was coated in black with high-temperature-resistant paint to enhance emissivity ($\varepsilon = 0.98$, according to the manufacturer [25]).

For the experimental approach, the PDMS block has lengths (L) of 65.0 mm, channel width (W_{ch}) of 5.0 mm, channel height (H_{ch}) of 5.0 mm, and distance between channels (W_p) of 6.3 mm. Fig. 3 shows the nominal dimensions of the PDMS serpentine.

Although the experimental setup contained a pressure transducer coupled to the system to perform the experimental pressure measurements, the instrument did not have the necessary precision to obtain reliable data. Furthermore, the uncertainty associated with the instrument was greater than the value of the data to be obtained. For this reason, a theoretical pressure prediction model was used. This theoretical model was then compared with the results obtained through numerical simulation. Throughout the discussion of the results, it will be

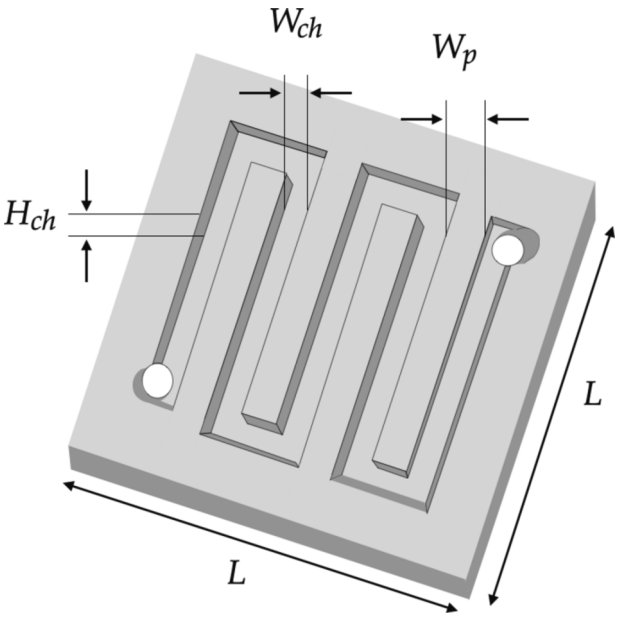

Fig. 3. PDMS serpentine scheme.

shown how this approach was able to provide a more accurate and reliable analysis of the pressure conditions within the system.

2.3.1. Experimental procedure and data reduction

In order to perform the experimental single-phase flow tests, the PDMS serpentine was initially filled with DI water, or the seaweed nanofluid, using a syringe pump. After filling, the pump was turned off, and the electrical resistance was triggered by increasing the system temperature. The tests were initiated when the surface temperature, measured by the thermocouple, reached 40 °C. All tests were performed using a constant heat flow, and three volumetric flow rates of 5, 10, and 15 ml/min were employed. The flow regime studied was laminar flow, as the maximum Reynolds number did not exceed 60 for both fluids studied. Additionally, the temperature of the liquid at the inlet was controlled by a refrigerated room maintained at 22 °C. The system acquired data at intervals of 5 values per second, and the last 200 points recorded in steady state were used for the processing and reduction of the experimental data, achieved through temperature measurements, when its variation was lower than the experimental uncertainties of the thermocouples.

A concentration of 0.1 wt% was chosen for the nanofluid to conduct the experimental flow tests. As presented below, theoretical models were used to compare the experimentally measured values for the thermal properties.

2.3.2. Theoretical models for the nanofluid thermal conductivity

In addition to experimental thermal conductivity measurements for the green nanofluid, values were compared using models and correlations obtained in the literature [26–28].

2.3.2.1. Thermal conductivity

$$k_{nf_{Maxwell}} = k_{bf}\left(\frac{k_{np} + 2k_{bf} + 2\varphi(k_{np} - k_{bf})}{k_{np} + 2k_{bf} - 2\varphi(k_{np} - k_{bf})}\right) \tag{1}$$

This equation represents the Maxwell model [28]. k_{np} and k_{bf} are the nanoparticle's thermal and base fluid thermal conductivity, respectively. At last, $k_{nf_{Maxwell}}$ represents the thermal conductivity for the nanofluid wishes by model.

Another model, by Hamilton and Crosser [28] expressed by Equation (2), considers the parameter relative to the shape of the particle, n, expressed by Equation (3). The shape factor, n, is a relation to the sphericity of the particle, w. Therefore, the sphericity of the particle varies with the shape; for instance, for a sphere, w = 3, and for a cylinder, w = 0.5.

$$k_{nf_{H\&C}} = k_{bf}\left(\frac{k_{np} + (n-1)k_{bf} - \varphi(n-1)(k_{bf} - k_{np})}{k_{np} + (n-1)k_{bf} + \varphi(k_{bf} - k_{np})}\right) \tag{2}$$

$$n = \frac{3}{w} \tag{3}$$

2.3.3. Pressure drop, thermographic analysis, and thermal performance

2.3.3.1. Pressure drop.

The theoretical single-phase liquid pressure drop is calculated using Equation (4), shown in the sequence, and the values are also used to compare with the numerical simulation.

$$\Delta p = f_{app}\frac{L}{D_h}\frac{\rho v^2}{2} \tag{4}$$

where f_{app} is friction factor data for hydrodynamically developing laminar flow given by Shah and London [29] and adjusted by the equation proposed by Churchill and Usagi [30]. A f_{app} covering developing and fully developed single-phase regions was derived experimentally by Copeland [23],

$$f_{app}Re = \left\{\left[3.2(L^+)^{-0.57}\right]^2 + (fRe)^2\right\}^{1/2} \tag{5}$$

where L^+ is the distance along the channel in the hydrodynamic entrance region, expressed by a non-dimensional axial coordinate:

$$L^+ = \frac{L}{ReD_h} \tag{6}$$

and f is the friction factor for fully developed laminar flow that is expressed by:

$$fRe = 19.64G + 4.7 \tag{7}$$

where G is a function of the channel aspect ratio, which is given by:

$$G = \left[\left(\frac{W_{ch}}{H_{ch}}\right)^2 + 1\right] / \left[\left(\left(\frac{W_{ch}}{H_{ch}}\right) + 1\right)^2\right] \tag{8}$$

2.3.3.2. Thermographic analysis.

The thermographic camera recorded the evolution of the surface temperature distribution around the central area of the steel sheet, as previously described in Fig. 1. More details about the data processing and calibration procedures can be found in our other works [25,31–33]. The camera has an analog-to-digital converter with a 14-bit resolution, assigning values from Analog-to-Digital Units (ADU) according to the intensity of the radiation. The operator can adjust the integration time, a parameter that allows the exposure time for each frame to be chosen. In this work, the integration time was set at 400 μs, which was considered sufficient to prevent pixel saturation from occurring in the operating temperatures range, as highlighted in [33].

2.3.3.3. Thermal performance.

The difference between the inlet and outlet temperatures of the flowing liquids was measured when they reached their steady state, and the same boundary conditions were used to compare the thermal heat capacity of each of the studied fluids.

2.3.4. Uncertainty analysis

To obtain the uncertainty of the dependent variables, the method described by Line and McClintock was used, which is described in Figliola and Beasley [34] by Equation (9):

$$u = \pm\sqrt{\left(\sum_{i=1}^{n}\theta_i u_{Xi}\right)^2} \tag{9}$$

where u is the absolute uncertainty of the dependent parameter, θ_i is the first partial derivative, and u_{Xi} represents the uncertainty of the independent parameters. For some equipment, such as the electric source and syringe pump, the uncertainties provided by the manufacturers were considered (Table 1). The experimental uncertainties of thermocouples were estimated using the method described by the Guide to express the uncertainty in measurements, GUM [35].

Table 1
Experimental uncertainties.

Variable	Uncertainty range
Contact angle, θ	± 0.1°
Pressure, Δp	±28*Pa*
Serpentine parameters, L, H_{ch}, W_{ch}, W_p	±0.05 mm
Temperature (thermocouples), T	± 0.3 °C
Temperature (thermographic camera), T	± 0.5 °C
Thermal conductivity, *k*	±5%
Viscosity, μ	±1%
Volumetric flow rate, Q	±0.035*ml*/*min*

2.4. Numerical approach

2.4.1. Numerical procedure

The ANSYS Fluent software was utilized for the numerical simulation due to its accuracy in modeling laminar flows and effectiveness in thermal simulations, and the laminar model was chosen to compute the flow velocity profiles in the serpentine. The laminar model was utilized due to the low Reynolds numbers applied to the tests. The study was conducted with the same inlet flow rate and temperature considered in the experimental tests. To the external walls of the experiment, we consider it adiabatic with the same temperature as the room where the experiments were conducted. We also consider 70 % of the power supply applied in the real experiment, corresponding to the difference between input power and heat losses observed in the system.

The issue being examined is numerically resolved by appropriately addressing the flow and heat transfer conservation equations. The continuity equation (mass conservation) applies to compressible and incompressible fluids and is represented by Equation (10).

$$\frac{\partial \rho}{\partial t} + \nabla \bullet (\rho u) = 0 \tag{10}$$

where u is the velocity vector, and ρ is the mass density of the fluid [36].

Equation (11) is the momentum conservation equation, which describes the motion of fluids during flow and is a non-linear partial differential equation.

$$\frac{\partial (\rho u)}{\partial t} + \nabla \bullet (\rho u \boldsymbol{u}) = -\frac{\partial p}{\partial \beta} + \nabla \bullet (\mu \nabla u) + S_M \tag{11}$$

where p is the static pressure, μ is dynamic viscosity, β represents the components from directions x, y and z, and S_M represents momentum source [36].

The energy equation to be solved takes the following form (Equation (12).

$$\frac{\partial (\rho i)}{\partial t} + \nabla \bullet (\rho i u) = -p \nabla \bullet u + \nabla \bullet (k \nabla T) + \Phi + S_i \tag{12}$$

where ρ is the density of the fluid, i is the internal energy, u is the velocity, p is the pressure, k is the thermal conductivity, T is the temperature, Φ is the dissipation function, and S_i is the additional source term [36]. The last one is the additional source term per unit volume per unit time, and it is associated with different effects that impact the fluid flow behaviour, including, for instance, chemical reactions in reactive flows and applied external forces. The term S_i is equal to $S_E - u.\, S_M$, where S_E is the energy source per unit volume per unit time, u is the fluid velocity, and S_M, is the already mentioned momentum source term.

The governing equations previously presented were numerically solved using the finite volume method combined with the coupled algorithm, where the equations are solved simultaneously, and the dependent variables are calculated at the cell centers.

2.4.2. Mesh validation

The Richardson extrapolation was employed to make the mesh validation based on an adaptation in the work of Roache and Knupp [37]. To this end, three meshes (coarse, medium, and fine) should be generated, with the number of elements increasing according to a constant geometric progression r, as indicated in Equation (13).

$$r \cong \frac{Finemeshelementsnumber}{Mediummeshelementsnumber} \cong \frac{Mediummeshelementsnumber}{Coursemeshelementsnumber} \tag{13}$$

The order of convergence p is calculated based on the parameters to be evaluated, obtained from each mesh Q and the previously calculated geometric constant, as observed in Equation (14).

$$p = \frac{\ln\left(\frac{Q_{coarse} - Q_{medium}}{Q_{medium} - Q_{fine}}\right)}{\ln(r)} \tag{14}$$

The equation describing the parameter considered exact by Richardson extrapolation is shown in Equation (15).

$$Q_{exact} = Q_{fine} - \frac{Q_{medium} - Q_{fine}}{r^p - 1} \tag{15}$$

Finally, the relative error ξ is the absolute value of the difference between the exact value and the value obtained from the finest mesh, as shown in Equation (16).

$$\xi = \left| 1 - \frac{Q_{fine}}{Q_{exact}} \right| \tag{16}$$

2.4.3. Computational model, mesh, and boundary conditions

The computational domain is shown in Fig. 4. The red solid represents the acrylic volume; the other is the PDMS. The fluid inlet and outlet can be observed without volume on the top. Between the acrylic and PDMS domains, there is a small AISI304 stainless steel sheet on which the heat power source was applied.

In order to fully define the situation under study, the boundary conditions must be defined. In the current study, all surfaces have a non-slip boundary condition applied, with the external surfaces being treated as adiabatic with the room temperature and the outlets having atmospheric pressure. More information about the surface boundary conditions can be found in Table 2.

The inlet fluid and ambient temperatures are based on the experimental conditions. 70 % of the power supply applied in the real experiment was considered for the numerical simulation. The standard software settings were used for water, and the properties of the materials and fluid are presented in Table 3.

Fig. 5 shows the mesh created to discretize the computational domain under study. The mesh geometry was carefully designed to ensure uniform division across the domain, emphasizing smooth connectivity between cells while maintaining orthogonality. The generated vertices were grouped into equal sets and selected together to ensure a consistent subdivision. Additionally, the face meshing command was applied to all faces to maintain the high quality of the mesh.

The mesh employed is orthogonal, non-uniform, and structured. A study of the non-interference of the mesh on the results was carried out, and the results are presented in Table 4. The mesh's aspect ratio, skewness, and orthogonality were used to validate its quality. The selected mesh was the number 1 mesh, which comprised 7 225 344 hexahedral elements.

The Richardson extrapolation was used, as described, to verify if the mesh with fewer elements is sufficiently accurate, and the results of the relative error are presented in Table 5.

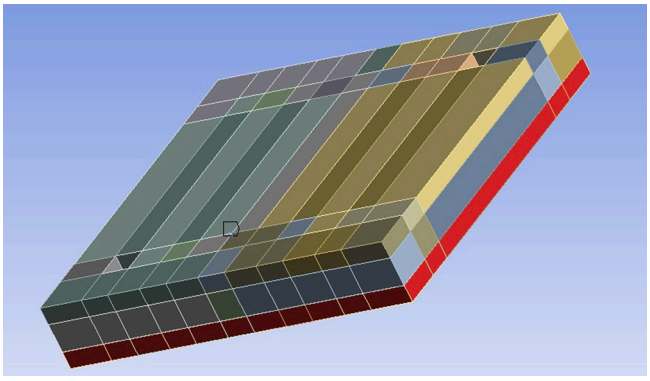

Fig. 4. Computational domain used.

Table 2
Surface boundary conditions.

Surface	Boundary Conditions
Fluid–Solid Interface	No-slip Interface and Convection
Interfaces between solid materials	Thermal Coupled
External surface	Adiabatic, room temperature (from experimental data)
Fluid inlet	Velocity Inlet (from experimental data)
Fluid outlet	Atmospheric pressure

Table 3
Thermophysical properties of the materials at 25 °C used in the simulation.

Properties	PDMS	Acrylic	AISI 304	GMNF	Ref.
Mass density (kg/m^3), ρ	970	1190	7900	998.20	[38–40]
Specific heat (J/kgK), c_p	1460	1470	500	4162.00*	[38,39,41]
Thermal conductivity (W/mK), k	0.20	0.19	16.30	0.641**	[24,36,39]
Viscosity (Pas)	NA	NA	NA	0.001003**	NA

* Value calculated according to[7].
** Value obtained experimentally.

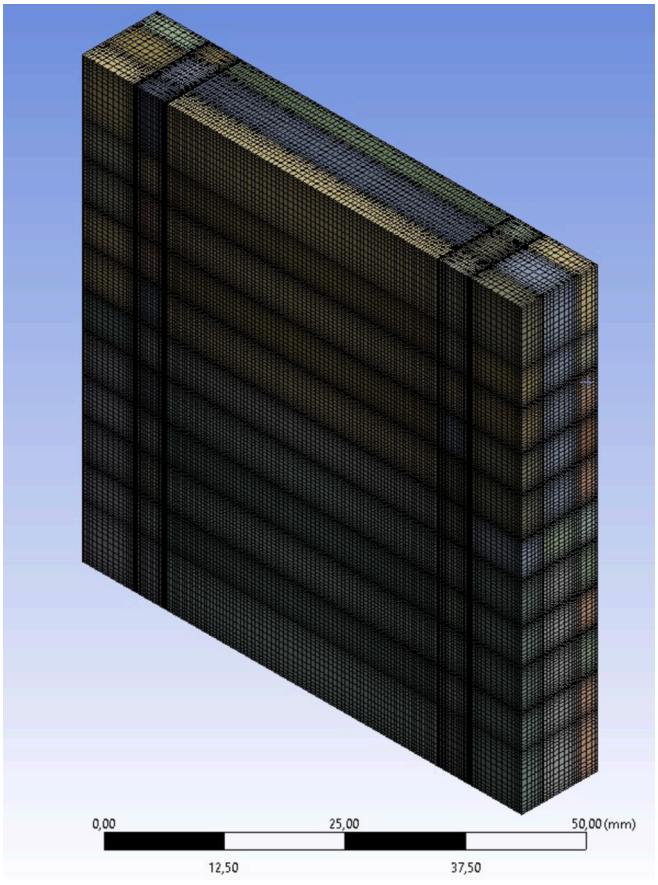

Fig. 5. Mesh used in the numerical simulation.

Table 4
Properties of the meshes that are employed in convergence.

	Mesh 1	Mesh 2	Mesh 3
Nodes	821,682	5,590,228	41,035,416
Elements	641,160	4,905,360	38,368,800
Minimum size (mm)	$9.45e^{-5}$	$1.96e^{-4}$	$3.88e^{-4}$
Maximum size (mm)	0.23	0.12	$5.77e^{-2}$
Aspect ratio	6.29	3.19	2.40
Skewness	$1.06e^{-2}$	$9.24e^{-3}$	$8.57e^{-3}$
Orthogonal quality	~1	~1	~1

Table 5
Validation mesh comparison with the exact result by Richardson Extrapolation.

	Outlet temperature	Inlet pressure	Surface temperature
Error	0.017	0.008	0.000

Table 6
Validation mesh comparison with experimental results.

	Outlet temperature (°C)	Inlet pressure (Pa)	Surface temperature (°C)
Error	±0.01	±0.05	±0.25

Table 6 showed that all analysed parameters did not present significant variation compared to the experimental results.

3. Results and discussion

3.1. Biosynthesis of Fe_3O_4 NPs and UV–vis spectroscopy

Analysis by UV–VIS spectroscopy of the aliquots studied in this work is presented in Fig. 6. The results showed that the maximum absorption intensity progressively increased with reaction time, indicating a continuous reduction of iron (III) chloride to Fe_3O_4 NPs. Notably, the absence of saturation in absorption intensity over the 6 h suggests that the synthesis reaction had not yet reached completion.

Moreover, a slight redshift observed from 349 nm (0.5 h) to 366 nm (6 h) implies potential modifications in the size and shape of Fe_3O_4 NPs. Such alterations are often associated with changes in polarity, and redshifts typically indicate a shift towards more polar (hydrophilic) environments. These findings may suggest the presence of algal biomolecules, such as polysaccharides, on the surface of the nanoparticles,

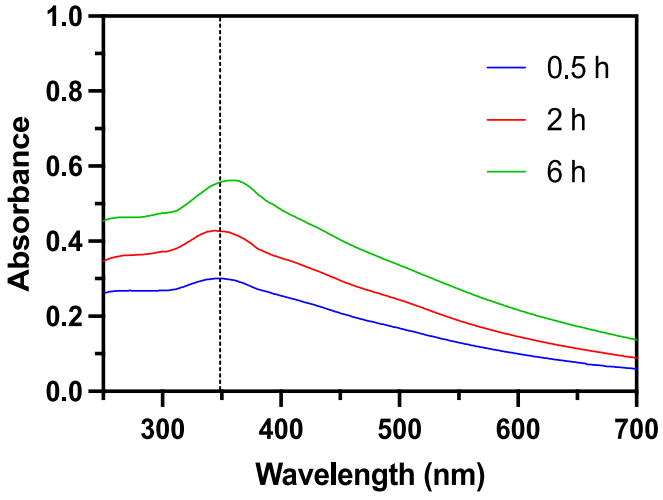

Fig. 6. UV–vis absorption spectra of time-dependent formation of Fe_3O_4 synthesized from *chlorella vulgaris* aqueous extract.

acting as effective capping agents. Capping agents, known for their hydrophilic nature, confer these properties to nanoparticles in an economical, stable, safe, biodegradable, and non-toxic manner [8,9,20].

3.2. Wettability

As illustrated in Fig. 7, wettability assessments reveal that incorporating green-synthesized magnetic nanofluid positively reduces the contact angle on glass and PDMS surfaces.

The glass and aluminium surfaces exhibit contact angles of less than 90°, indicating a hydrophobic condition. This result suggests that the surface interacts more effectively with the fluid. In studies related to two-phase flow and boiling in pools, such behaviour typically leads to improved heat transfer [10].

On the PDMS surface, the green nanofluid shows a contact angle with hydrophobic characteristics but has lower values than pure water.

3.3. Viscosity

The viscosity findings concerning the shear rate are depicted in Fig. 8. Alongside the base fluid (water), the results are displayed for each tested concentration. A marginal rise in fluid viscosity relative to water is evident. A slight increase was noted regarding the correlation between viscosity and nanoparticle concentration, particularly pronounced between the concentrations from 0.05 to 0.1 wt%.

Despite meticulous procedures during data acquisition and the execution of three tests for each sample, the results showed no significant variations. However, sedimentation of nanoparticles was observed in the samples, particularly evident in those with higher nanoparticle concentrations. An example of the sedimentation observed at the centre of the plate is depicted in Fig. 9.

3.4. Stability test results

Fig. 10 shows the qualitative analysis of nanoparticle sedimentation using, as base fluid, the DI-Water (left side) or algae extract (right side). After preparation, both the traditional Fe_3O_4 nanofluid and the Fe_3O_4 nanofluid produced from algae extract were ultra-sonicated for 1 h and left to rest. Following a protocol similar to one presented in another study by the group [42], the sedimentation was qualitatively evaluated by obtaining optical images of colloidal dispersions at 0, 2, and 5 h after sample preparation.

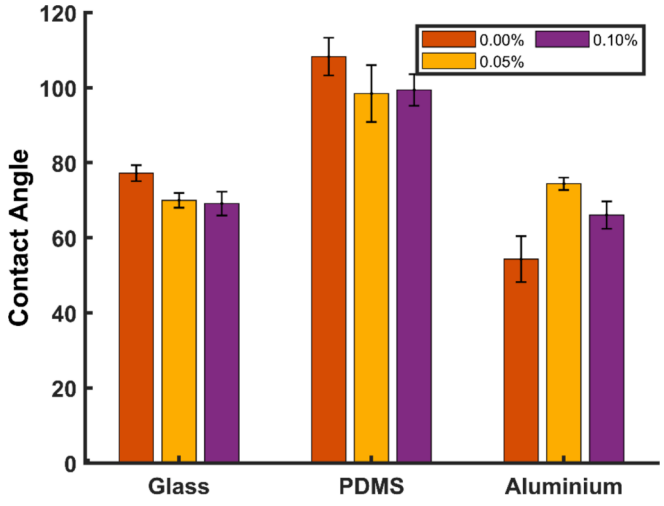

Fig. 7. Contact angle on glass, PDMS, and aluminum substrate for Green Magnetic Nanofluid (GMNF) at different concentrations. (For interpretation of the references to color in this figure legend, the reader is referred to the web version of this article.)

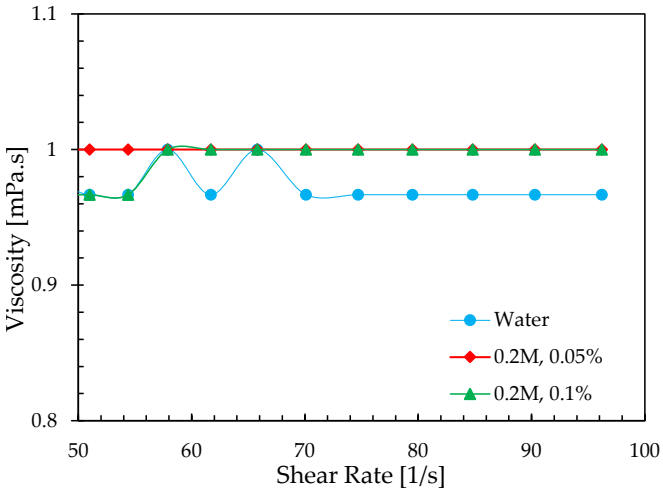

Fig. 8. Viscosity as a function of shear rate for GMNF.

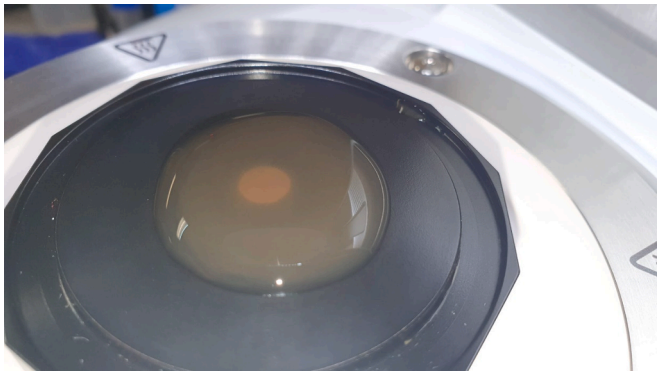

Fig. 9. GMNF sample in the rheometer with nanoparticle sedimentation in the center after taking measurements.

The images of the nanoparticle sedimentation obtained over the analyzed time interval showed distinct evolutions. Initially, at t = 0h, nanofluids are distinguished only by their characteristic coloration. The nanofluid produced from the algae extract is yellowish, which can be attributed to various organic components present in the extract. It may also be influenced by the type of particles used to produce it. Meanwhile, the conventional nanofluid is dark black.

For the other two intervals of 2 h and 5 h, the traditional nanofluid began to lose color, becoming transparent, while the green nanofluid was less influenced. In both cases, it was possible to perceive the sedimentation of nanoparticles at the bottom of the container; however, the deposition in the case of the traditional nanofluid was at least twice as much as that of the green nanofluid. Another interesting aspect to observe is that the amount of iron nanoparticles adhered to the walls of the container was quite evident in the traditional nanofluid. These results suggest a promising potential for testing these fluids in devices that require heat exchange with heated surfaces in flow.

3.5. Thermal conductivity

Adding NPs into water affects thermal conductivity differently, depending on the amount. Small amounts, such as 0.05 wt% were found to decrease thermal conductivity, as illustrated in Fig. 11. However, for a concentration higher than the previous one, 0.10 wt%, the thermal conductivity surpassed that of pure water. Thus, this nanofluid concentration was chosen for flow tests to ensure performance superior to the base fluid, minimizing sedimentation effects and ensuring low

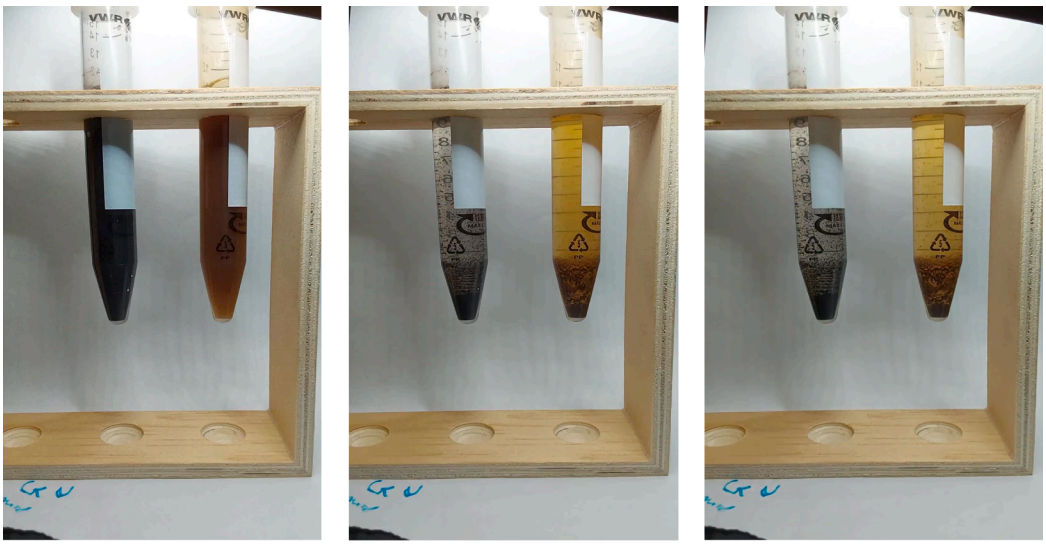

Fig. 10. Qualitative analysis of nanoparticle sedimentation in the nanofluids over 5 h for the concentration of 0.1%. In all images, the conventional nanofluid made from iron nanoparticles added to base fluid DI-Water is on the left, and the nanofluid made from iron nanoparticles and algae extract is on the right.

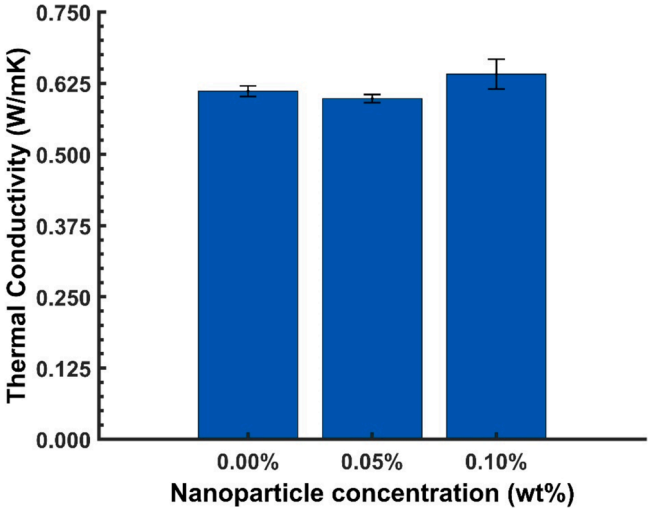

Fig. 11. Variation of thermal conductivity in the nanofluid as a function of nanoparticle percentage.

production costs.

Regarding the experimental results, for the concentration of 0.05 %, the amount of nanoparticles is so small that the equipment does not have sufficient sensitivity to detect fluctuations, presenting values within the instrument's margin of error, similar to those of DI-Water. Additional investigations and high-precision equipment are necessary to detect these small variations, as suggested by Roque *et al.* [43]. Souza *et al.* [44] also highlighted the complexity of measuring nanofluids and parameters that can lead to errors, such as aggregation and sedimentation. Another phenomenon that may help to explain the lower average value is the issue raised by Wu *et al.* [45], who demonstrated that, for sensors based on the transient source method, the measurement of fluid thermal conductivity is affected by thermal convection, which occurs due to the operating principle of the sensor. This phenomenon can artificially increase the measured thermal conductivity of fluids, particularly those with low viscosity. With the increase in viscosity at the 0.05 % concentration, as observed in Fig. 8, the influence of thermal convection may have decreased, resulting in a lower measured thermal conductivity. However, this likely does not reflect the changes induced by adding nanoparticles. Otherwise, a downward trend in thermal conductivity would be expected.

The experimentally obtained results were also compared with the theoretical models of Maxwell and Hamilton & Crosser (H&C), commonly used for predicting the thermal conductivity of nanofluids [18]. Table 7 shows consistency in the experimental results, with a difference of approximately 2 % compared to the theoretical results for the 0.05 wt% concentration, where the measured value was lower than predicted by the correlations. In contrast, for the 0.1 wt% nanoparticle concentration, the experimental results were about 4.5 % higher than those provided by the models and around 6.4 % higher than the base fluid measured.

3.6. Fluid flow characteristics

For the experiments to evaluate the liquid flow characteristics and its thermal transfer capacity, which will be discussed below, a nanofluid concentration of 0.1 wt% was selected.

3.6.1. Pressure drop results

The comparison of the pressure drop obtained by Copeland's theoretical model (Equation (4) with the values obtained by simulation is shown in Fig. 12. As expected, the results show an increase in pressure drop as the amount of liquid passing through the serpentine channel increases. Additionally, the curves exhibit similar trends regardless of the type of fluid passing through the region. The green nanofluid (red line) has a slightly higher pressure drop than DI-Water (black line), about 5 % higher, a small variation given that the nanofluid concentration is 0.1 wt%. This result allows us to infer that, within one margin of security, the effect of the nanofluid on pressure drop is not detrimental to the system, which is an important parameter as it defines the energy consumption required for pumping the cooling system.

The simulated results showed almost no difference between the

Table 7
Comparison between experimentally measured results and theoretical models.

Concentration (%wt)	Measured (W/mK)	Maxwell model (W/mK)	Relative error (%)	H&C model (W/mK)	Relative error (%)
0.05	0.5980	0.6117	2.30	0.611	2.19
0.10	0.6410	0.6126	−4.42	0.6113	−4.62

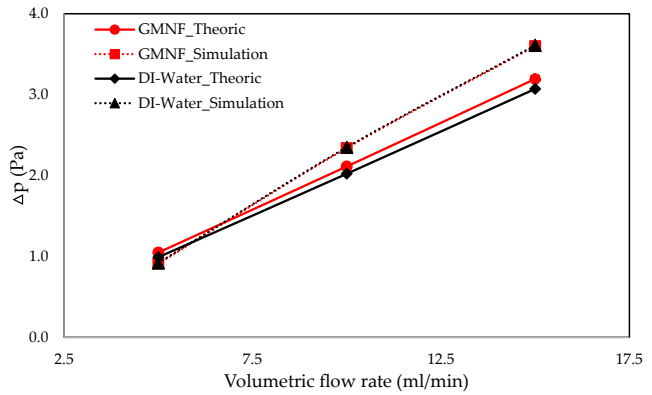

Fig. 12. Comparison of theoretical correlation *vs.* simulation for pressure drop as a function of volumetric flow rate.

fluids and a good agreement with the theory results, especially at low volumetric flow rates. At the biggest volumetric flow rate tested, the error was around 10 %.

The proximity between the simulated values for water and nanofluid may be associated with the properties of the liquids. For pressure drop, viscosity is the main parameter influencing this behavior. Viscosity affects flow resistance and, consequently, pressure loss. Although the studied nanofluid has a slightly higher viscosity than water, about 5 %, in our case, the obtained difference may not have been sufficient to cause a significant variation in pressure drop, a value also proven by the theoretical model.

3.7. Heat transfer characteristics

3.7.1. Thermographic results

The thermographic image observations help understand how different fluids affect surface temperature distribution in the serpentine system. The thermal camera obtained the temperature gradients, with the flow direction going from right to left, as shown in Fig. 13. The serpentine channel, through which the fluid flows, is in the center, and the top and bottom edges represent the sides of the PDMS serpentine. As the flow rate increases, temperatures decrease for both cases, indicating that the fluid is cooling more rapidly.

Fig. 14 compares the surface temperature gradients of the images obtained experimentally by the thermographic camera with the simulation results. If the experimental images between DI-Water and the green nanofluid, Fig. 14a and 14c, respectively, are compared, the green nanofluid maintains a more homogeneous temperature, which is positive. This suggests a better heat distribution compared to DI-Water. The superior thermal properties of the nanofluid allow for more efficient heat exchange. The nanoparticles improve convection in the fluid and seem to suggest the same in conduction in PDMS. This result is evident when comparing images of both fluids at a flow rate of 5 ml/min. In the images, it is observed that, for DI-Water flow (Fig. 14a), there are regions of the heat exchanger with temperature gradients close to the initial test's values, around 39 °C, while for the nanofluid flow, the gradients are much milder (Fig. 14c).

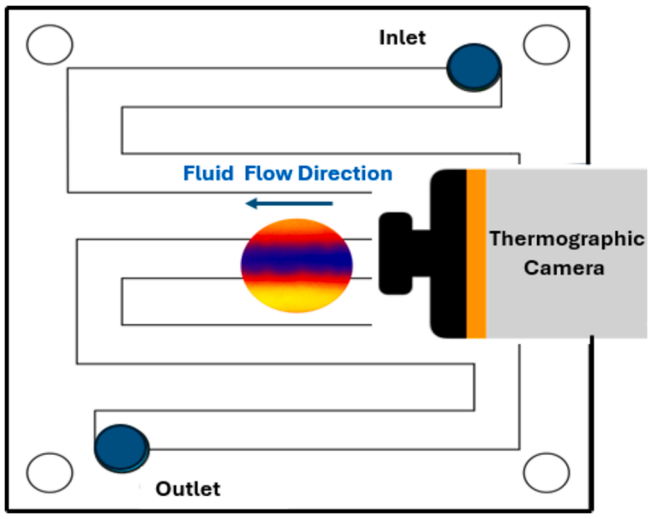

Fig. 13. Observable serpentine area by the thermography camera.

For the temperature gradients obtained through numerical simulation, as shown in Fig. 14b and 14d, the temperature distributions are smoother than those obtained experimentally. Although the temperatures at the sides of the heat exchanger are lower than the thermal camera images (Fig. 14a and 14b), the effect is more pronounced when DI-Water flow is used. In the case of the green nanofluid, the match is closer for the surface temperature profile, as illustrated in Fig. 14c and 14d.

In the numerical simulation, heat is uniformly transmitted to the electric heater steel stainless sheet, while experimentally, this condition cannot be guaranteed due to potential thermal losses to the surroundings. Assuming this condition, the green nanofluid, with higher thermal conductivity than the base fluid, has a greater capacity to exchange heat with the heated surface. This effect is responsible for the closer alignment between the observed gradients and those simulated.

3.8. Thermal performance results

The difference between the inlet and outlet temperatures of the fluids flowing through the PDMS heat sink is shown in Fig. 15. The graph presents the experimental results compared to those obtained from numerical simulation.

Regarding the experimental data, the largest temperature difference occurs for the green nanofluid, indicating that the amount of energy absorbed by it is greater than that absorbed by DI water. Another significant result was observed at a 5 ml/min flow rate. In this case, it is noted that the amount of heat absorbed by the nanofluid is higher than the flow rates of 10 and 15 ml/min. These results demonstrate that the amount of liquid pumped through the serpentine channel impacts the thermal capacity of the heat exchanger. An identical behavior, derived from experimental tests, was also observed for nanofluids flowing in microchannels, as reported in [32,46].

Regarding the results obtained from the simulations, there was virtually no variation between them, a behavior similar to that observed for pressure drop, as shown in Fig. 12. In this specific case, this is likely due to the limitations of finite volume methods in evaluating phenomena in nanofluid heat transfer, such as Brownian motion, nanoparticle shapes, and distribution, among others, as also observed by other researchers [47].

4. Conclusions

The present study addressed the synthesis process of magnetic iron oxide nanoparticles using *Chlorella vulgaris* extract. The results demonstrated that, even at low concentrations, using green-synthesized magnetic nanofluids (GMNFs) did not significantly compromise the fluid's viscosity, enhancing thermal conductivity and improving flow characteristics. This demonstrates the considerable potential of GMNFs for thermal applications requiring heat transfer, both in single-phase systems and, potentially, in two-phase systems.

Based on the analyses carried out in this work, some important conclusions can be drawn:

- The UV–Vis spectroscopy analysis indicated that the synthesis of Fe_3O_4 NPs revealed the presence of algal biomolecules, such as

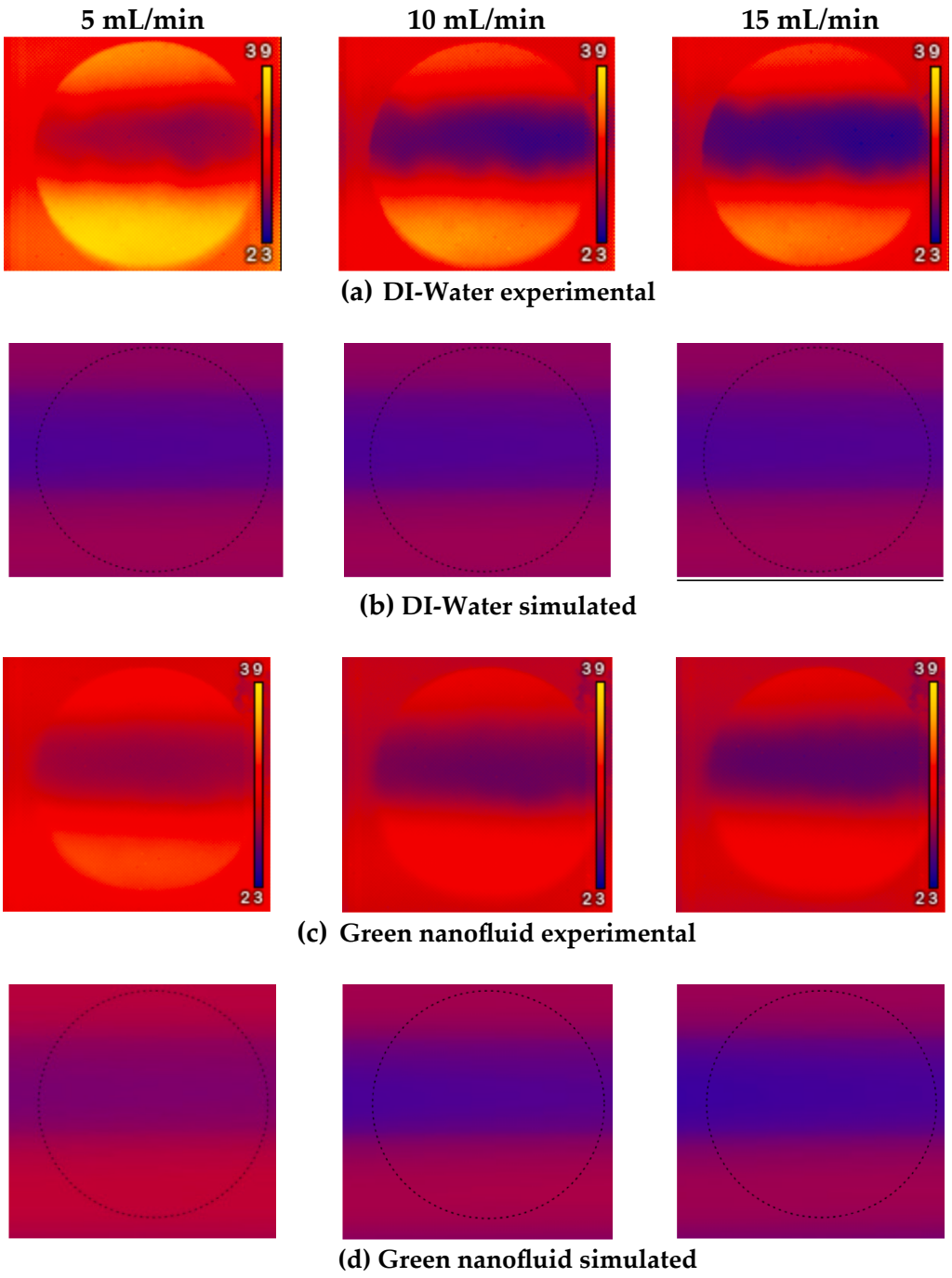

Fig. 14. Surface temperature gradients obtained experimentally by the thermal camera *vs.* numerical simulation. **(a)** surface temperature from DI-Water flow obtained experimentally by thermographic camera, **(b)** surface temperature from DI-Water flow obtained by numerical simulation, **(c)** surface temperature from green nanofluid flow obtained experimentally by thermographic camera, **(d)** surface temperature green nanofluid flow obtained by numerical simulation. (For interpretation of the references to color in this figure legend, the reader is referred to the web version of this article.)

polysaccharides, on the nanoparticle surface. These biomolecules act as hydrophilic capping agents, contributing to the nanoparticles' stability, safety, and biodegradability;

- The incorporation of a green-synthesized magnetic nanofluid reduces the contact angle on glass and PDMS surfaces, enhancing wettability, which could lead to enhanced heat transfer;
- The results show an increase in the nanofluid viscosity, averaging about 5 %, with more significant sedimentation at 0.1 wt%. Similar viscosity increase levels were also verified in [14];
- The qualitative sedimentation analysis showed that the green nanofluid, derived from algae extract, exhibits lower sedimentation level and nanoparticle adhesion over time compared to the classic Fe_3O_4 nanofluid.
- For the nanofluid with a concentration of 0.1 wt%, the experimental results were approximately 4.5 % higher than the numerical ones and about 6.4 % higher than the base fluid experimental results. The deviation percentage levels between the experimental and numerical results were also verified in other published studies, for instance, in [15];
- The results obtained by the theoretical model show that the green nanofluid presents slightly higher pressure drops compared to DI-

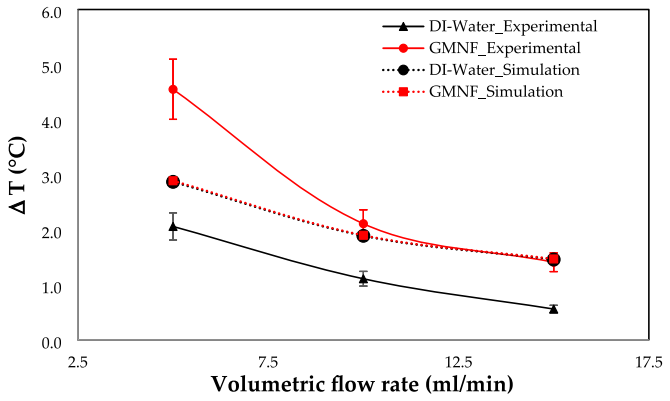

Fig. 15. Experimental data *vs.* simulation results for the temperature difference between the inlet and the outlet for the tested fluids at the proposed PDMS serpentine device.

Water (around 5 %), minimally impacting the pressure loss of the nanofluid;

- The simulated pressure drop results for the base fluid and the nanofluid did not show significant differences. This is likely due to the minor difference between the properties of the two used fluids, as the simulation results did not account for factors such as nanoparticle distribution, Brownian motion, size, or shape;
- Experimentally, as the flow rate increases, the temperatures decrease, indicating an effective cooling; the green nanofluid maintains a more uniform temperature distribution than DI-Water, enhancing the heat exchange efficiency;
- For the numerical simulation, the temperature distributions are smoother than those obtained experimentally with the thermal camera in both cases;
- The experimental findings confirmed that the largest inlet/outlet temperature difference occurs with the green nanofluid, indicating greater energy absorption compared to DI- Water.

CRediT authorship contribution statement

Glauco Nobrega: Writing – original draft, Methodology, Investigation, Conceptualization. **Reinaldo Souza:** Writing – review & editing, Writing – original draft, Supervision, Software, Methodology, Formal analysis, Data curation, Conceptualization. **Beatriz Cardoso:** Writing – original draft, Validation, Investigation, Formal analysis, Conceptualization. **Inês Afonso:** Investigation, Formal analysis, Data curation. **José Pereira:** Writing – review & editing, Writing – original draft, Investigation. **Elaine Cardoso:** Writing – review & editing, Supervision, Methodology. **Ana Moita:** Writing – review & editing, Validation, Supervision, Software. **João Ribeiro:** Writing – review & editing, Supervision, Resources, Project administration, Methodology. **Rui Lima:** Conceptualization, Funding acquisition, Methodology, Project administration, Resources, Supervision, Writing – review & editing.

Declaration of competing interest

The authors declare that they have no known competing financial interests or personal relationships that could have appeared to influence the work reported in this paper.

Acknowledgments

The authors are grateful to the Fundação para a Ciência e a Tecnologia (FCT), Avenida D. Carlos I, 126, 1249–074 Lisboa, Portugal, for partially financing the Project “Estratégias interfaciais de arrefecimento para tecnologias de conversão com elevadas potências de dissipação”, Ref. PTDC/EMETED/7801/2020). José Pereira also acknowledges FCT for his PhD Fellowship (Ref. 2021. 05830.BD). The authors are also grateful for FCT funding through 2022.03151.PTD (https://doi.org/10.54499/2022.03151.PTDC), 2022.06207.PTDC (https://doi.org/10.54499/2022.06207.PTDC) and LA/P/0083/2020 IN + -IST-ID. The authors also acknowledge the partial financial support within the R&D Units Project Scope: UIDB/04077/2020, UIDP/04077/2020, UIDB/00532/2020, and LA/P/0045/2020 (ALiCE). Glauco Nobrega was supported by the PRT/BD/153088/2021 doctoral grant financed by the Portuguese Foundation for Science and Technology (FCT), and with funds from MCTES/República Portuguesa, under the MIT Portugal Program. A.S. Moita also acknowledges FCT for partially financing her contract through CEECINST/00043/2021/CP2797/CT0005, doi: 10.54499/CEECINST/00043/2021/CP2797/CT0005. The authors are grateful to Professor Andrea Zille for providing materials and equipment and their technical support.

Data availability

Data will be made available on request.

References

[1] G. Nobrega, B. Cardoso, R. Souza, J. Pereira, P. Pontes, S.O. Catarino, D. Pinho, R. Lima, A. Moita, A review of novel heat transfer materials and fluids for aerospace applications, Aerospace 11 (2024).
[2] I.S. Afonso, G. Nobrega, R. Lima, J.R. Gomes, J.E. Ribeiro, Conventional and recent advances of vegetable oils as metalworking fluids (MWFs): a review, Lubricants 11 (2023).
[3] S. Purree, M. Nadeem, A. Shahzad, H.M. Ali, Synthesis, heat transfer properties and stability of nanofluids for commercialization: a review, Chem. Eng. Commun. 210 (2023) 814–836, https://doi.org/10.1080/00986445.2021.1976163.
[4] A.H. Pordanjani, S. Aghakhani, M. Afrand, M. Sharifpur, J.P. Meyer, H. Xu, H. M. Ali, N. Karimi, G. Cheraghian, Nanofluids: physical phenomena, applications in thermal systems and the environment effects- a critical review, J. Clean. Prod. 320 (2021) 128573, https://doi.org/10.1016/j.jclepro.2021.128573.
[5] R. Kamatchi, S. Venkatachalapathy, B. Abhinaya Srinivas, Synthesis, stability, transport properties, and surface wettability of reduced graphene oxide/water nanofluids, Int. J. Therm. Sci. 97 (2015) 17–25, https://doi.org/10.1016/j.ijthermalsci.2015.06.011.
[6] I.S. Afonso, B. Cardoso, G. Nobrega, G. Minas, J.E. Ribeiro, R.A. Lima, Green synthesis of nanoparticles from olive oil waste for environmental and health applications: a review, J. Environ. Chem. Eng. 12 (2024) 114022, https://doi.org/10.1016/j.jece.2024.114022.
[7] R.R. Souza, F.M. Sá Barbosa, G. Nobrega, E.M. Cardoso, J.C.F. Teixeira, A.S. Moita, R. Lima, An innovative PDMS cell to improve the thermal conductivity measurements of nanofluids, Therm. Sci. Eng. Prog. 42 (2023) 101926, https://doi.org/10.1016/j.tsep.2023.101926.
[8] S. Ying, Z. Guan, P.C. Ofoegbu, P. Clubb, C. Rico, F. He, J. Hong, Green synthesis of nanoparticles: current developments and limitations, Environ. Technol. Innov. 26 (2022) 102336, https://doi.org/10.1016/j.eti.2022.102336.
[9] D. Sharma, S. Kanchi, K. Bisetty, Biogenic synthesis of nanoparticles: a review, Arab. J. Chem. 12 (2019) 3576–3600, https://doi.org/10.1016/j.arabjc.2015.11.002.
[10] X. Yin, C. Hu, M. Bai, J. Lv, Molecular dynamic simulation of rapid boiling of nanofluids on different wetting surfaces with depositional nanoparticles, Int. J. Multiph. Flow 115 (2019) 9–18, https://doi.org/10.1016/j.ijmultiphaseflow.2019.03.022.
[11] Pereira, J.; Souza, R.; Moita, A.; Moreira, A. Nanofluids and Ionic Fluids as Liquid Electrodes: An Overview on Their Properties and Potential Applications. *Processes* 2023, *11*.
[12] R.R. Souza, I.M. Gonçalves, R.O. Rodrigues, G. Minas, J.M. Miranda, A.L. N. Moreira, R. Lima, G. Coutinho, J.E. Pereira, A.S. Moita, Recent advances on the thermal properties and applications of nanofluids: from nanomedicine to renewable energies, Appl. Therm. Eng. 201 (2022) 117725, https://doi.org/10.1016/j.applthermaleng.2021.117725.
[13] Ajeeb, W.; Zhang, J.Z.; Wu, Z.; Murshed, S.M.S.; Sundén, B. Numerical Development of the Thermal Convection Characteristics of Nanofluids. In *Fundamentals and Transport Properties of Nanofluids*; Murshed, S.M.S., Ed.; The Royal Society of Chemistry, 2022; p. 0 ISBN 978-1-83916-419-4.
[14] W. Ajeeb, S.M.S. Murshed, Numerical study of convective heat transfer performance, entropy generation and energy efficiency of Al and Al_2O_3 Nanofluids in Minichannel, J. Nanofluids 12 (1) (2023), https://doi.org/10.1166/jon.2023.1903.
[15] W. Ajeeb, S.M.S. Murshed, Comparisons of Numerical and Experimental Investigations of the Thermal Performance of Al_2O_3 and TiO_2 Nanofluids in a Compact Plate Heat Exchanger, Nanomaterials 12 (2022), https://doi.org/10.3390/nano12203634.

[16] W. Ajeeb, S.M.S. Murshed, Characterization of Thermophysical and Electrical Properties of SiC and BN Nanofluids, Energies 16 (9) (2023) 3768, https://doi.org/10.3390/en16093768.
[17] Z. Khattak, H.M. Ali, air cooled heat sink geometries subjected to forced flow: a critical review, Int. J. Heat Mass Transf. (2019).
[18] I. Gonçalves, R. Souza, G. Coutinho, J. Miranda, A. Moita, J.E. Pereira, A. Moreira, R. Lima, Thermal conductivity of nanofluids: a review on prediction models, controversies and challenges, Appl. Sci. 11 (2021).
[19] S.Y. Jung, J.H. Park, S.J. Lee, H. Park, Heat transfer and flow characteristics of forced convection in PDMS microchannel heat sink, Exp. Therm. Fluid Sci. 109 (2019) 109904, https://doi.org/10.1016/j.expthermflusci.2019.109904.
[20] YP, Y.; Shameli, K.; Miyake, M.; Kuwano, N.; NB, B.A.K.; SE, B.M.; KX, L. Green Synthesis of Magnetite (Fe3O4) Nanoparticles Using Seaweed (Kappaphycus Alvarezii) Extract. PG - 276 LID - 10.1186/S11671-016-1498-2 [Doi] LID - 276.
[21] R. Rajkumar, G. Ezhumalai, M. Gnanadesigan, A green approach for the synthesis of silver nanoparticles by chlorella vulgaris and its application in photocatalytic dye degradation activity, Environ. Technol. Innov. 21 (2021) 101282, https://doi.org/10.1016/j.eti.2020.101282.
[22] H. Khanehzaei, M. Ahmad, K. Shameli, Z. Ajdari, Synthesis and Characterization of Cu@Cu2O Core Shell Nanoparticles Prepared in Seaweed Kappaphycus Alvarezii Media, Int. J. Electrochem. Sci. 10 (2015) 404–413.
[23] Copeland, D. Optimization of Parallel Plate Heatsinks for Forced Convection. In Proceedings of the Sixteenth Annual IEEE Semiconductor Thermal Measurement and Management Symposium (Cat. No.00CH37068); 2000; pp. 266–272.
[24] R.R. Souza, F.M. Sá Barbosa, G. Nobrega, E.M. Cardoso, J.C.F. Teixeira, A.S. Moita, R. Lima, Experimental Study of an Innovative Elastomer-Based Heat Exchanger, Case Stud Therm. Eng. 49 (2023) 103365, https://doi.org/10.1016/j.csite.2023.103365.
[25] E. Teodori, P. Pontes, A.S. Moita, A.L.N. Moreira, Thermographic analysis of interfacial heat transfer mechanisms on droplet/wall interactions with high temporal and spatial resolution, Exp. Therm. Fluid Sci. 96 (2018) 284–294, https://doi.org/10.1016/j.expthermflusci.2018.03.013.
[26] M. Pavlik, The Dependence of Suspension Viscosity on Particle Size, Shear Rate, and Solvent Viscosity. (2011).
[27] C. Pang, J.W. Lee, Y.T. Kang, Review on combined heat and mass transfer characteristics in nanofluids, Int. J. Therm. Sci. 87 (2015) 49–67, https://doi.org/10.1016/j.ijthermalsci.2014.07.017.
[28] B. Lamas, B. Abreu, A. Fonseca, N. Martins, M. Oliveira, Critical analysis of the thermal conductivity models for CNT based nanofluids, Int. J. Therm. Sci. 78 (2014) 65–76, https://doi.org/10.1016/j.ijthermalsci.2013.11.017.
[29] Shah, R.K.; London, A.L. Chapter V - Circular Duct. In; Shah, R.K., London, A.L.B. T.-L.F.F.C. in D., Eds.; Academic Press, 1978; pp. 78–152 ISBN 978-0-12-020051-1.
[30] S.W. Churchill, R. Usagi, A general expression for the correlation of rates of transfer and other phenomena, AIChE J. 18 (1972) 1121–1128, https://doi.org/10.1002/aic.690180606.
[31] G. Marseglia, M.G. De Giorgi, P. Pontes, R. Solipa, R.R. Souza, A.L.N. Moreira, A. S. Moita, Enhancement of microchannel heat sink heat transfer: comparison between different heat transfer enhancement strategies, Exp. Therm. Fluid Sci. 150 (2024) 111052, https://doi.org/10.1016/j.expthermflusci.2023.111052.
[32] Maia, I.; Rocha, C.; Pontes, P.; Cardoso, V.; Miranda, J.M.; Moita, A.S.; Minas, G.; Moreira, A.L.N.; Lima, R. Heat Transfer and Fluid Flow Investigations in PDMS Microchannel Heat Sinks Fabricated by Means of a Low-Cost 3D Printer. In; Ren, Y., Ed.; IntechOpen: Rijeka, 2020; p. Ch. 8 ISBN 978-1-78984-419-1.
[33] G. Marseglia, M.G. De Giorgi, D.S. Carvalho, P. Pontes, R.R. Souza, A.L.N. Moreira, A.S. Moita, Experimental investigation on the effects of the geometry of microchannels based heat sinks on the flow boiling of HFE-7100, Appl. Therm. Eng. 236 (2024) 121479, https://doi.org/10.1016/j.applthermaleng.2023.121479.
[34] Figliola, R.S.; Beasley, D.E. *Theory and Design for Mechanical Measurements*; 4th ed.; Wiley: New York SE - xvi, 542 pages : illustrations ; 26 cm + 1 card (13 x 13 cm), 2006; ISBN 9780471445937; 0471445932.
[35] GUM, Bureau International Des Poids Et Mesures; Organization Internationale De Normalisation-Guide to the Expression of Uncertainty in Measurement, International Organization for Standardization (2008).
[36] Versteeg, H.K.; Malalasekera, W. *An Introduction to Computational Fluid Dynamics: The Finite Volume Method*; Hall, P., Ed.; London, 2007.
[37] P.J. Roache, P.M. Knupp, Completed Richardson extrapolation, Commun. Numer. Methods Eng. 9 (1993) 365–374, https://doi.org/10.1002/cnm.1640090502.
[38] Specification Sheet: Alloy 304/304L Available online: https://www.sandmeyersteel.com/images/Alloy304-304L-APR2013.pdf (accessed on 31 July 2024).
[39] Acrylic Properties Available online: https://www.ipolymer.com/pdf/Acrylic.pdf (accessed on 31 July 2024).
[40] LH, C.; TE, K.; RE, G.; AF, P.; Rubinstein, M.; DA, W. Soft Poly(Dimethylsiloxane) Elastomers from Architecture-Driven Entanglement Free Design. PG - 5132-40 LID - 10.1002/Adma.201502771 [Doi].
[41] 6.777J/2.751J Material Property Database Available online: https://www.mit.edu/~6.777/matprops/pdms.htm (accessed on 31 July 2024).
[42] R.R. Souza, V. Faustino, J.D. Oliveira, I.M. Gonçalves, J.M. Miranda, A.S. Moita, A. L.N. Moreira, J.C.F. Teixeira, M. Bañobre-López, R. Lima, A Novel and Extremely Stable Nanofluid Based on Iron Oxide Nanoparticles: Experimental Investigations on the Thermal Performance, Therm. Sci. Eng. Prog. 26 (2021) 101085, https://doi.org/10.1016/j.tsep.2021.101085.
[43] D. Roque, W. Ajeeb, S.M.S. Murshed, J.M.C. Pereira, Forced convection heat transfer characteristics of Al2O3 nanofluids in a minichannel - an experimental study, J. Phys. Conf. Ser. 2116 (2021) 12056, https://doi.org/10.1088/1742-6596/2116/1/012056.
[44] R.R. Souza, V. Faustino, I.M. Gonçalves, A.S. Moita, M. Bañobre-López, R. Lima, A review of the advances and challenges in measuring the thermal conductivity of nanofluids, Nanomater. 12 (2022).
[45] K.-F. Wu, T.-F. Cao, W.-B. Li, H. Zhang, G.-H. Tang, Quantitative evaluation of the natural convection effect on thermal conductivity measurement with transient plane source method, Case Stud. Therm. Eng. 45 (2023) 102933, https://doi.org/10.1016/j.csite.2023.102933.
[46] R. Chein, J. Chuang, Experimental microchannel heat sink performance studies using nanofluids, Int. J. Therm. Sci. 46 (2007) 57–66, https://doi.org/10.1016/j.ijthermalsci.2006.03.009.
[47] Ullah, A.; Kilic, M.; Habib, G.; Sahin, M.; Khalid, R.Z.; Sanaullah, K. Reliable Prediction of Thermophysical Properties of Nanofluids for Enhanced Heat Transfer in Process Industry: A Perspective on Bridging the Gap between Experiments, CFD and Machine Learning. *J. Therm. Anal. Calorim.* **2023**, *148*, 5859–5881, doi: 10.1007/s10973-023-12083-7.